Influence of hydrophobic treatment on the structure of compressed gas diffusion layers

C. Tötzke[a,b,*], G. Gaiselmann[c], M. Osenberg[a], T. Arlt[a], H. Markötter[a], A. Hilger[a,d], A. Kupsch[e], B.R. Müller[e], V. Schmidt[c], W. Lehnert[f,g], I. Manke[a]

[a] Helmholtz-Zentrum Berlin für Materialien und Energie GmbH, 14109 Berlin, Germany

[b] Universität Potsdam, 14476 Potsdam, Germany

[c] Universität Ulm, 89069 Ulm, Germany

[d] Technische Universität Berlin, 10623 Berlin, Germany

[e] BAM Bundesanstalt für Materialforschung und -Prüfung, 12200 Berlin, Germany

[f] Forschungszentrum Jülich, 52425 Jülich, Germany

[g] RTWH Aachen University, 52062 Aachen, Germany

*corresponding author: Email christian.toetzke@helmholtz-berlin.de
Phone +49331 977 2966
Fax +49331 977 2092

Abstract

Carbon fiber based felt materials are widely used as gas diffusion layer (GDL) in fuel cells. Their transport properties can be adjusted by adding hydrophobic agents such as polytetrafluoroethylene (PTFE). We present a synchrotron X-ray tomographic study on the felt material Freudenberg H2315 with different PTFE finishing. In this study, we analyze changes in microstructure and shape of GDLs at increasing degree of compression which are related to their specific PTFE load. A dedicated compression device mimicking the channel-land pattern of the flowfield is used to reproduce the inhomogeneous compression found in a fuel cell. Transport relevant geometrical parameters such as porosity, pore size distribution and geometric tortuosity are calculated and consequences for media transport discussed. PTFE finishing results in a marked change of shape of compressed GDLs: surface is smoothed and the invasion of GDL fibers into the flow field channel strongly mitigated. Furthermore, the PTFE impacts the microstructure of the compressed GDL. The number of available wide transport paths is significantly increased as compared to the untreated material. These changes

improve the transport capacity liquid water through the GDL and promote the discharge of liquid water droplets from the cell.

Keywords: gas diffusion layer, synchrotron tomography, compression, hydrophobic treatment, water transport

1. Introduction

The gas diffusion layer (GDL) is a key component for the liquid water and gas transport in polymer membrane fuel cells (PEFCs) [1-4]. It features a porous transport structure that allows the transfer of reactant gases from the flowfield channels to the electrodes and the concurrent removal of liquid water produced at the catalyst layer. At the same time, the GDL must keep the membrane humidified to maintain its proton conductivity. Careful adjustment of water transport and storage capacity of the GDL material is, therefore, an important aspect of fuel cell water management. There exist several types of carbon fiber based GDL materials with distinct microstructures. For instance, carbon paper GDLs consist of randomly orientated straight fibers, while the microstructure of carbon felt materials is characterized by curved fibers with random orientation. In contrast, carbon cloth GDLs are made of a woven carbon tissue, i.e. possess a regular microstructure. In general, the transport properties of a GDL are closely linked to its microstructure and can, furthermore, be adjusted by suitable finishing procedures. In particular, the application of hydrophobic additives such as PTFE as well as the addition of a micro porous layer (MPL) are common strategies to tune the transport behavior according to the requirements of specific applications. Precise understanding of the functionality requires, therefore, detailed knowledge about the GDL morphology including the spatial distribution of hydrophobic additives. In a fuel cell the GDL compression is a function of the clamping force. The influence of compression on fuel cell behavior is shown in [5, 6].

Neutron [7-26] and X-ray [27-42] imaging are suitable noninvasive tools to investigate water and other liquid media in porous materials such as GDLs [43-52]. Neutrons have high penetration depths into most metals while they are very sensitive to hydrogen at the same time [53-56]. High resolution synchrotron absorption X-ray tomography provides excellent imaging conditions to analyze the microstructure of GDLs three-dimensionally [57-64]. In a previous

paper, we reported on the impact of inhomogeneous compression on the microstructure of a carbon fiber-based felt material (GDL type H2315 produced by Freudenberg FFCCT) [65].

The present work covers a high-resolution synchrotron X-ray tomographic study on PTFE coated GDL materials (Type H2315 T10A and H2315 T20A produced by Freudenberg). While focusing on the same carbon felt material, the actual scope is to analyze the influence of hydrophobic treatment on shape and microstructure of inhomogeneously compressed gas diffusion layers including the evaluation of its potential consequences for the liquid water and gas transport.

2. Methods and Materials

2.1. Imaging conditions

The experiments were performed at the synchrotron light source BESSY II (Helmholtz-Zentrum Berlin /Germany) using the tomography station of the BAMline [66]. The imaging conditions were adapted to the previous study of compressed GDLs [65, 67]: A W-Si multilayer monochromator with an energy resolution of $\Delta E/E=10^{-2}$ was used to turn the white synchrotron X-ray beam into a monochromatic beam. The beam energy was adjusted to 15 keV where contrast for fiber material was optimal. A PCO camera (4008 × 2672 pixels) in combination with a lens system and a 20 µm thick CWO scintillator screen provided a pixel resolution of 0.88 µm, i.e. a respective physical spatial resolution of about 2 µm, capturing a field of view of 3.6 × 2.3 mm^2 [68]. The incident beam was narrowed to the field of view by a slit system in order to avoid detector backlighting [69]. A sample holder bearing circular GDL samples of 3mm diameter was mounted on a translation/rotation stage. During tomography, the sample was stepwise rotated over an angular range of 180°. A radiographic set of 1500 projections and 500 flat-field images was acquired and subsequently reconstructed to a 3D image volume. The exposure time was 2.5 s plus 1.7 s read-out time for a single radiograph adding up to an acquisition time of 140 min for an entire tomogram.

2.2. Sample compression device

A dedicated compression device designed and constructed at Forschungszentrum Jülich was used to provide well-defined compression conditions during tomography.

A detailed description and illustration of the compression tool is provided by Tötzke et al. [70]. The main components of the device are a base unit with a circular platform (Ø 3 mm) on which the sample is placed on and the main compression unit including the compression punch. The main unit is fastened to the top of the base element allowing for quick and easy exchange of GDL samples. A 0.8 mm wide and 1.0 mm deep channel profile was manufactured into the punch to mimic the channel-land-pattern of the flowfield, thus reproducing the local pressure conditions found in a fuel cell. Vertical positioning of the punch with an accuracy of about ±5 µm, allowed for precise adjustment of the GDL compression.

2.3. Materials

H2315 is a nonwoven, carbon fiber-based felt material produced by the company Freudenberg FFCCT. It is used as standard GDL in many fuel cells where its physical properties are adapted to the requirements of the respective application, e.g. by adding water proofing compound. The present investigation focusses on the influence of PTFE finishing on microstructure and shape of GDLs. Two PTFE treated H2315 GDL types, T10A and T20A containing 10 wt.% and 20 wt.% PTFE, were chosen and compared to the untreated material. The thickness as specified by the manufacturer at precompression of 0.025 MPa are Z=218 µm, 212 µm and 216 µm for H2315 (without PTFE), H2315 T10A and H2315 T20A, respectively. The precompression is applied to create a plain and smooth GDL surface needed for the thickness determination. Further manufacturer specifications for the GDL materials under study can be found in the supplementary material (see table S1).

Circular samples with a diameter of 3 mm were prepared and placed in the compression device. High resolution synchrotron X-ray absorption tomograms were acquired at four different degrees of compression: 0 vol.%; 10 vol.%; 20 vol.% and 30 vol.%. The actual compression values do slightly deviate ($\Delta C \leq 1.4\%$) due to the accuracy limits of punch adjustment ($\leq \pm$ 5 µm). For all sample H2315 the initial thickness underneath land of Z_0 was successively reduced to Z_{10}, Z_{20} and Z_{30} with corresponding degrees of compression of C_0, C_{10}, C_{20} and C_{30}. The actual values for Z and C as measured in the reconstructed sample volumes are stated in Table 1. Note that we refer to manufacture specification of Z when calculating the degree of compression.

Table 1. Thickness (Z) of GDL underneath land and the corresponding degree of compression (C) summarized for all samples.

Type	Z_0 / µm	Z_{10} / µm	Z_{20} / µm	Z_{30} / µm	C_0 / vol.%	C_{10} / vol.%	C_{20} / vol.%	C_{30} / vol.%
H2315	219	194	177	151	-0.46	11.01	18.81	30.73

H2315 T10A	215	191	169	150	-1.42	9.91	20.28	29.25
H2315 T20A	215	193	171	153	0.46	10.64	20.83	29.17

3. Results and Discussion

In this section, we present a synchrotron tomographic analysis of compressed carbon felt GDL materials with different PTFE finish. The influence of the hydrophobic agent on shape and microstructure of GDL is evaluated and implications for the water and media transport are discussed. Two samples H2315 T10A and T20A containing 10 and 20wt.% PTFE, respectively, are measured and compared with the untreated basis material H2315 which was already analyzed in a precedent study [65].

3.1 Fiber structure and PTFE distribution

To begin with, samples are considered in uncompressed state. In figure 1, 0.5 × 0.5 mm^2 large sections of the different GDLs were rendered to provide a three-dimensional impression of their microstructure. Each row contains a perspective view onto top (right column) and bottom surface (left column) of the respective sample. At first glance, the general similarity in microstructure is obvious reflecting the fact that all samples are made of the same felt type material (H2315). Fibers are randomly orientated and have a diameter of about 10µm. They are curved predominantly in in-plane (x-y) direction. However, the fiber entanglement in z-direction, which is necessary to provide the fiber structure with mechanical stability, is also visible in the virtual cross sections (side planes x-z and y-z).

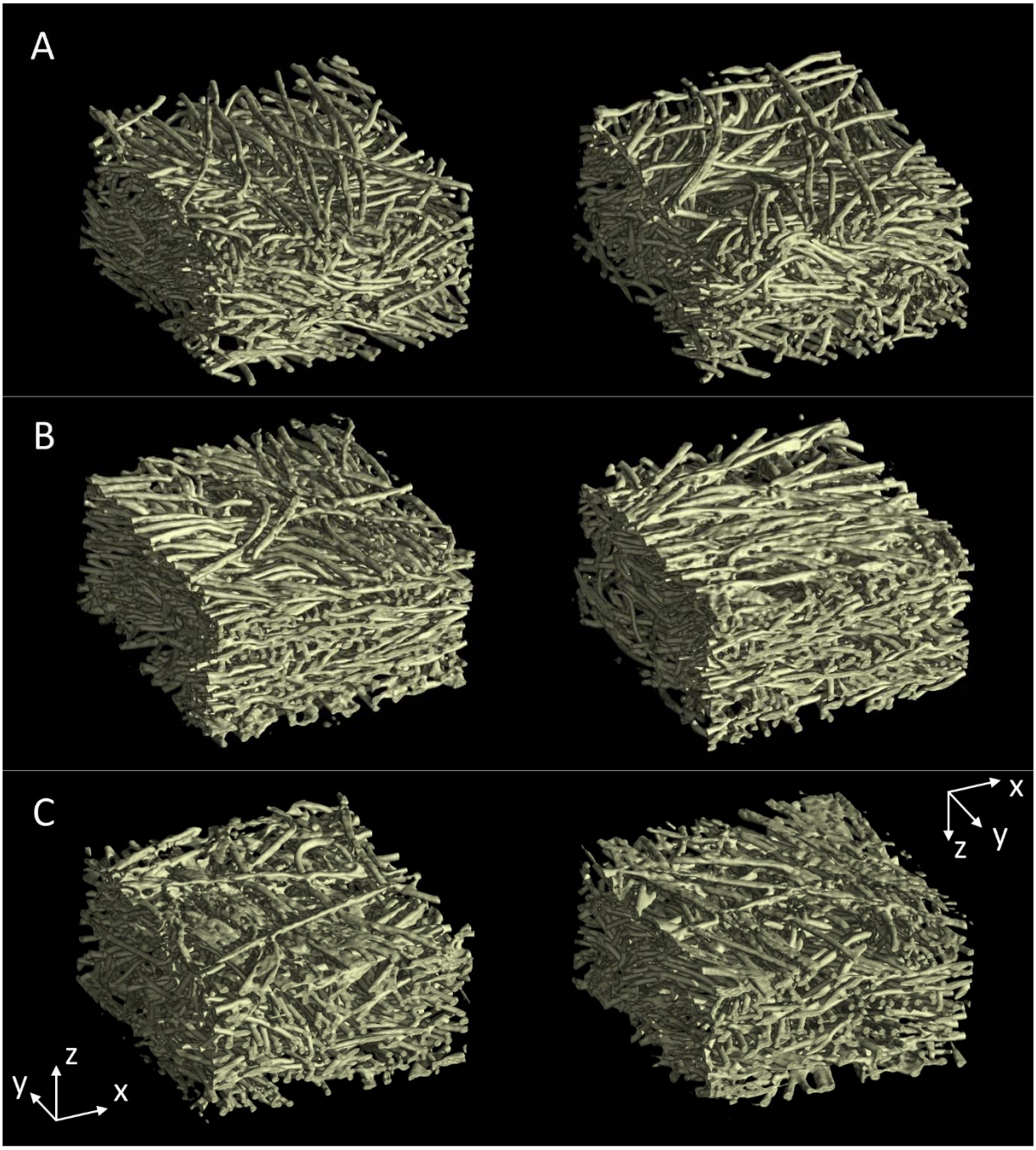

Figure 1. Perspective views onto bottom (left column) and top surface (right column) of considered GDL samples in the uncompressed state. 0.5 × 0.5 mm2 large sections are rendered in 3D. A: H2315 – no PTFE, B: H2315 T10A – 10 wt.% PTFE, C H2315 T20A – 20 wt.% PTFE.

The untreated material (see figure 1 A) is free of PTFE, binder or other additives. Top and bottom surface look very similar. Fibers packaging appears regular suggesting uniform geometric transport conditions in z-direction. Figure 1 B displays the microstructure of H2315 T10. Taking into account the fiber dimension of Ø 10µm, the spatial resolution (pixel size 0.88

$\times$ 0.88 μm^2) and inherent occurrence of moderate phase contrast at fiber edges, it is not feasible to unambiguously identify ultra-thin PTFE coats covering individual fibers. However, PTFE agglomerated on and in between fibers is clearly visible. Figure 1 indicates that the hydrophobic agent is not uniformly distributed within the sample. While little PTFE is detectable at the bottom it appears to form an adhesive film on the top face (see figure 1 B right) creating a smoother material surface. Compared to the untreated material the fiber packaging of T10A appears slightly denser, i.e. the porosity is lower. Figure 1 C shows the rendered section of H2315 T20A. On both top and bottom side a PTFE coat is clearly visible. Looking at cross section (the virtual cutting planes at the side) it appears that PTFE is not uniformly distributed but concentrated in the surface-near material layers. Fiber packaging is comparable to that of H2315 T10A.

In order to clearly resolve PTFE coating on the individual fiber level we take advantage of the superior resolution of scanning electron microscopy (SEM). As 2D-method it can be used to study the surface of samples. Figure 2 shows top and bottom face of the PTFE-treated materials at increasing factors of magnification. Especially at the highest magnification the PTFE phase can be very clearly distinguished from fibers (see right column of figure 2). The images reveal that individual fibers are not completely covered by a continuous PTFE film. The hydrophobic agent rather tends to agglomerate in between fibers. These agglomerates either glue fiber junctions or form thin films stretching out between adjacent fibers with parallel orientation and connecting them to fiber strands. In some case these films are partially torn and detached from the fiber surface, which apparently happens during drying (and shrinking) of PTFE precursor subsequent to the coating procedure. As visible in figure 2 D a great portion of the individual fiber surfaces remain clear of coating even at locations with high PTFE concentrations. Figure 2 provides a direct comparison of H2315 T10 and T20A showing the top and bottom sides, respectively. The top side of both materials has a very similar degree of coating (figure 2 A vs. C). On the bottom side (figure 2 B vs. D), the situation is different. While only little PTFE is present at T10A the fibers of T20A are heavily agglutinated due to the large amount of PTFE present in the near-surface region. In contrast to the top face agglutination of fibers seems not to be constricted to the upmost fiber layers but continues inwards the material.

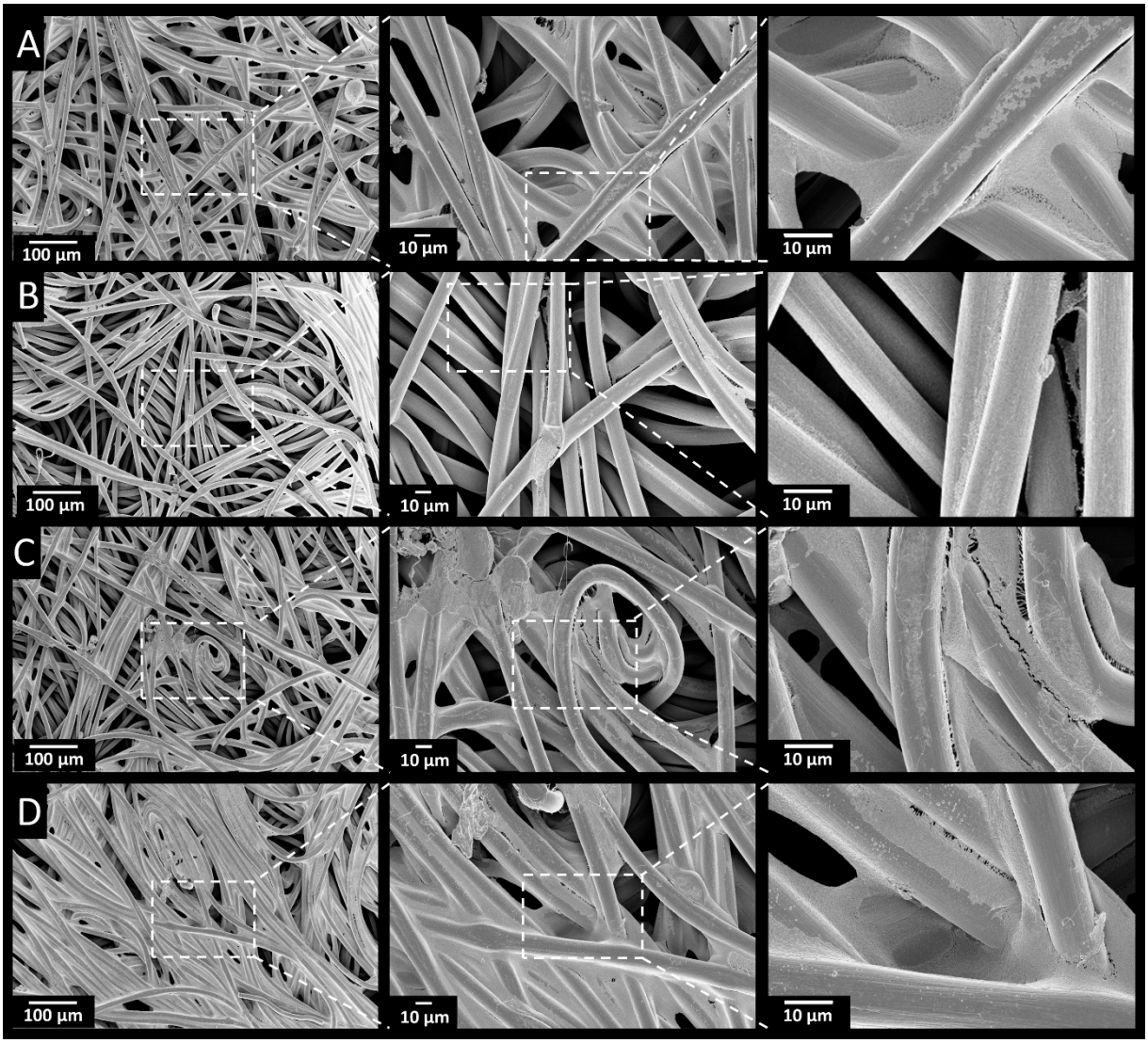

Figure 2. SEM image series of top and bottom sides of PTFE-treated materials at increasing factors of magnification. A + B: H2315 T10A top + bottom side, C + D: H2315 T20A top + bottom side.

The qualitative analysis of PTFE distribution can be extended to three dimensions by considering the in-plane porosity of respective materials at different depths (z). Differences in local porosity between H2315 T10, T20A and the untreated material can be interpreted in terms of pore space filled up with PTFE. In figure 3 B the local porosity is plotted when passing through materials from bottom up. All graphs show a steep increase (starting at distance of about $\leq$ 20 µm from top or bottom, respectively) within surface near regions indicating that fiber density plummets when approaching the very edge of material. This can be considered as common geometrical boundary effect (note fiber diameter of 10 µm) that applies for all samples. Comparing the bulk phase of considered materials the course of porosity differs markedly. The bulk porosity of H2315 is about 0.75 with local deviations smaller than 0.05. For H2315 T10A a pronounced minimum is found in 20 µm distance to the top surface (z=185 µm). In this layer,

porosity is about 10% lower as compared to the untreated material suggesting that about 13 % of initial pore space has been filled up with PTFE. Within the bottom and central part of the sample ($z < 125$ µm) local porosity roughly coincides with the graph of H2315 indicating that this region only contains very little PTFE. Two distinct minima of local porosity are found in H2315 T20A, the sample with the highest PTFE load, in 40 µm distance to top and 25 µm to bottom surface, respectively. Porosity within top region appears similar to that of H2315 T10A suggesting a comparable PTFE distribution. In contrast to T10A, local porosity in the bottom half of T20A is significant lower than in the top half (3% on average) indicating the majority of PTFE being deposited in the bottom region ($z \leq 100$ µm). The minimum at $z = 40$ µm points to the layer with highest PTFE concentration. These results are in very good accordance with the visual impressions provided by the 3D-rendered volumes (figure 1), the radiographic views in through plane perspective as provided by figure 3 A and the SEM images (figure 2). The reason for this uneven distribution might be due to the coating and drying process [4]. A plot of local porosity of the different GDL samples compressed underneath land is provided in the supplementary material (see figure S2).

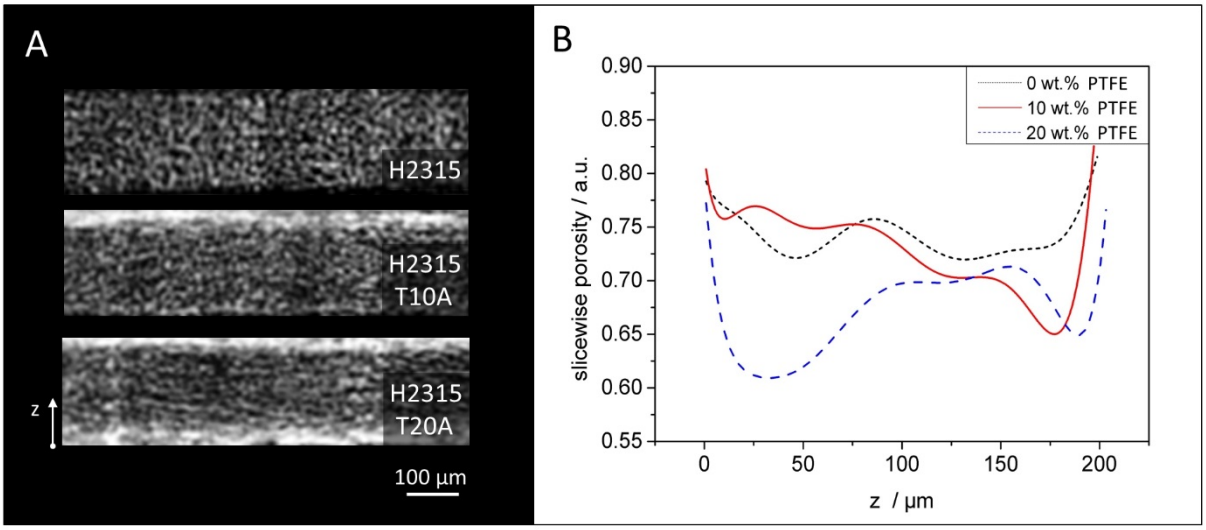

Figure 3. A: Radiographs of considered materials aligned in through-plane direction. Bright near-surface regions indicate high local PTFE concentration. B: Local porosity (in x-y plane) at different material depth (plotted from bottom up).

3.2 Changes of shape – Channel invasion by GDL fibers

In the next step we study the influence of different PTFE loads on the shape of the inhomogeneously compressed GDLs. More precisely, we consider the progressive extension of fiber material into the flowfield channel as result of increasing GDL compression.

An overview on the different sample at the four considered degrees of compression is provided in the supplementary materials (see figure S1).

The image series clearly illustrates the interactions of punch and sample (see also figure 5). While all samples are homogenously compressed underneath the ribs (according to adjusted punch position and corresponding degree of compression) the GDL material is less compressed within the channel region and extends into the channel volume. This applies to all samples, however, to a different extend. Figure 4 shows a better resolved representative section of the different samples at the highest compression.

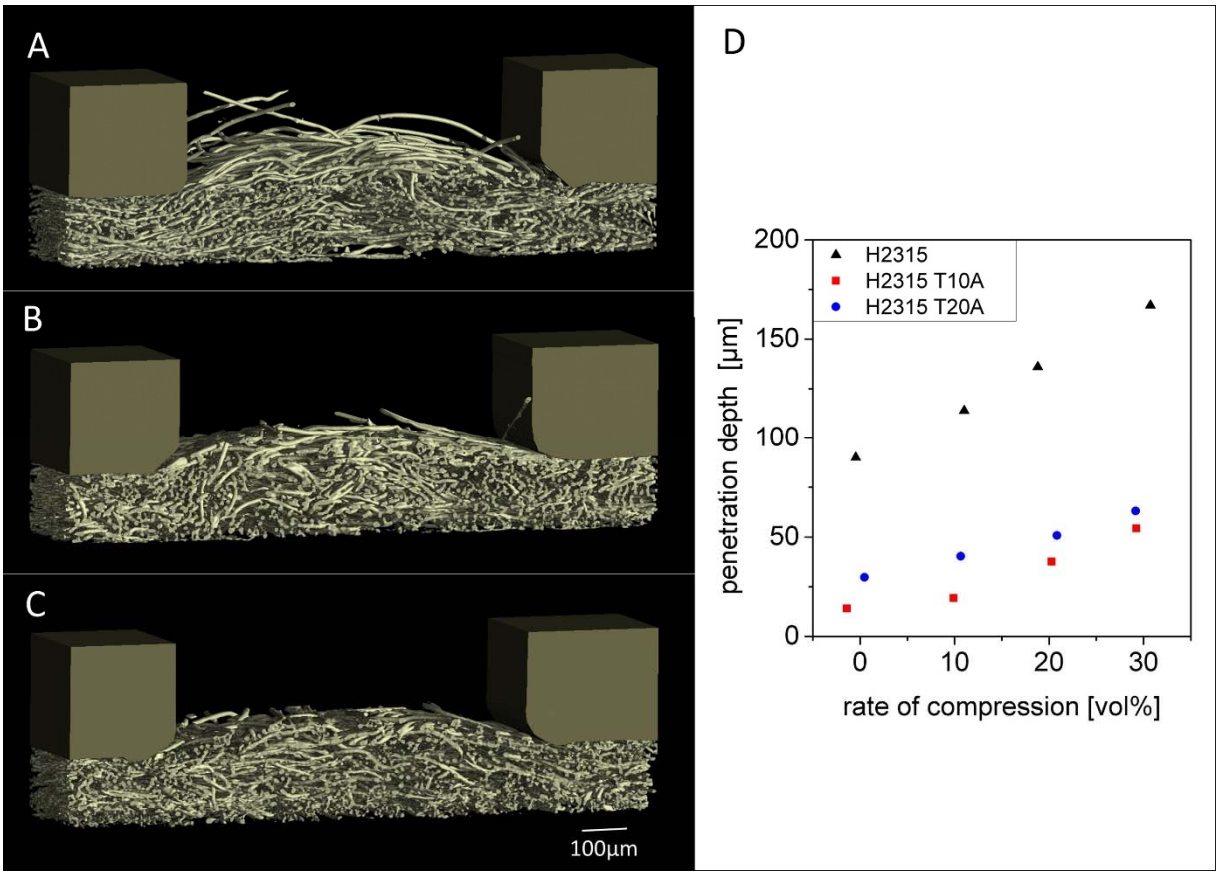

Figure 4. Perspective 3D- view on the sample compressed by about 30 vol.%, rendered on a section of channel and the adjacent land area. A: H2315 (no PTFE); B: H2315 T10A (10 wt.% PTFE); C H2315 (20 wt.% PTFE). D: Penetration of the flowfield channel by fiber material measured along the center line of the channel at increasing rates of compression.

The depicted 3D-volumes with dimensions of 1.35 × 0.4 x 0.25 mm^3 comprise sample regions located underneath channel and the adjacent land area including a part of channel and land volume above. As already reported in [65] fibers of untreated GDL H2315 (see figure 4 A) extend far into the channel volume (almost 170 µm deep along the center line of channel). Individual loose fiber endings even protrude farther, some of them reaching penetration depths of nearly 300 µm. Loose fiber endings are bent at the edges of the flowfield channel profile and

tilt up with increasing degree of compression. These fibers have the potential to impede the removal of liquid excess water from the cell as they form obstacles for moving water droplets in the flowfield channels. These droplets are driven the convection gas stream towards the outlet to be ejected from the cell. Deceleration or stoppage of droplets promotes water agglomerations or even flooding events in the channel. Concerning the opposite material side one should also consider the risk of membrane perforation that protruding fibers endings could carry.

Figure 4 documents that the protrusion of GDL is much less pronounced in the case of PTFE-treated material. Penetration depths at maximum compression measured along the center line of the channel are 54 and 63 µm for T10A and T20A, respectively, which is only about one third of that of the untreated H2315. The altered protrusion behavior can be assigned to the PTFE film deposited within the surface region. It acts like a binder: adjoining fibers with similar local orientation are agglutinated to form strands and fiber junctions are glued to adhesive joints. This enhances the mechanical strength of the fibers construction as it is known from carbon fiber composite materials. Strength enhancement of the near-surface layers counteracts the expansion and deformation of the top face of the GDL and, therefore, strongly mitigates invasion of fiber material into the channel volume. Moreover, it almost completely prevents protrusion of loose fiber endings. The very similar protrusion of behavior of T10A and T20A appears reasonable as the local PTFE distribution in the top regions is comparable.

3.3. Transport relevant parameters of microstructure: porosity, pore size distribution, geometrical tortuosity

In this section major results of the geometric analysis of microstructure are presented while further information on the analyzing procedures can be found in the supplementary material and the literature referenced herein. We investigated the influence of inhomogeneous compression by the flowfield punch on the local microstructure of GDL comparing the PTFE finished samples with the untreated material. Transport-relevant geometrical parameters such as porosity, pore size distribution or tortuosity were calculated for regions located underneath channels and land, respectively. In the following we refer to these regions as "land region" and "channel region". Size and position of the analyzed sub-regions are illustrated in figure 5. The dimensions of the two land regions in H2315 T10A are 350 × 1577 × z μm^3, respectively, where parameter z denotes the thickness, which is adjusted according to the increasing compression (0 vol.%, 10 vol.%, 20 vol.%, 30 vol.%): z is 188 µm, 165 µm, 145 µm and 125 µm. The dimension of the corresponding regions in H2315 T20A are 350 × 1577 × z μm^3, with z = 182 µm, 163 µm, 140 µm and 125 µm.

In contrast to land areas, the local thickness of the GDL material in the channel region strongly depends on the distance to the channel edge. The maximum thickness is found at the channel center from where it continuously decreases towards the channel edges. We analyzed geometric properties of these region within a sub-volume of 525 × 1577 × 184 μm^3 in the case of H2315 T10A and 525 × 1577 ×193 μm^3 in the case of H2315 T20A. These volumes were thoroughly filled with GDL material for all the compression stages under study.

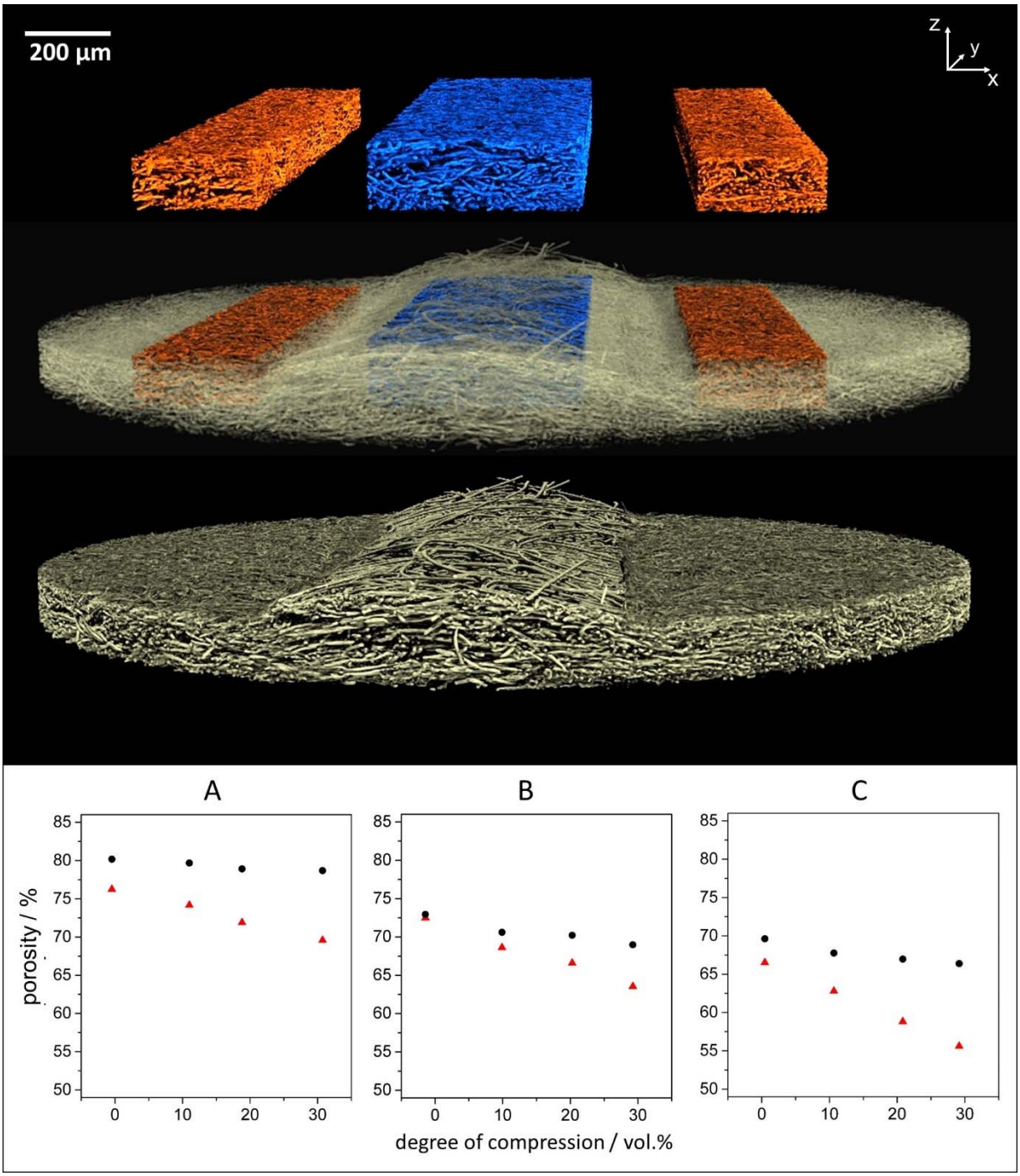

Figure 5. Top: Visualization of GDL sub-volumes analyzed: Illustration of size and position within the sample (H2315 T10A, degree of compression 30 vol.%). The land regions are highlighted in red, the channel region in blue. Bottom:Porosity of different GDL materials calculated for regions underneath channel (black circles) and land (red triangles) at different degrees of compression. A: H2315; B: H2315 T10A; C: H2315 T20A.

The porosity of the three GDL samples within both land and channel region at different degrees of compression is displayed in figure 5 at bottom. The difference in porosity between the two areas in the uncompressed state of H2315 and H2315 T20A (figure 5 A and C) is due to the precompression of the sample during preparation as explained in section 2.3. In contrast, the

same porosity is measured in the channel and land region of H2315 T10A revealing insufficient precompression as the actual degree of compression was only C_0 = -1.42) (c.f. figure 5 B). The porosity underneath the land decreases according to the reduction of the pore volume by the compression punch. In contrast, underneath the flowfield channel, were the GDL material is not in direct contact with the compression punch, the porosity decreases only moderately.

An important geometric characteristic of porous materials is the pore size distribution (PSD). In fiber structures, the entire pore space is interconnected and cannot be segmented into individual pores due to the lack of a physical criterion. For this reason, we analyze the pore structure in terms of the continuous pore size distribution (cPSD), which does not consider pores as discrete objects but treats the entire pore structure as continuum. The cPSD describes the fraction of the pore volume P(r) that can be covered by spheres with a radius r, such that these spheres do not overlap with the solid (fiber) phase. P(r) is calculated as a normalized volume with respect to the entire volume and, therefore, $\lim_{r\to 0} P(r)$ = porosity. For a more detailed mathematical description of the cPSD we refer to [71, 72].

Figure 6 provides an overview on cPSD of the different GDL materials at the compression stages under study. Results of land regions are displayed in top row, channel region in the bottom row. As general observation is that progressing material compression of land regions shifts the entire cPSD towards smaller pore radii and reduces its maximum value which reflects the respective decrease in porosity. The corresponding graphs for the channel regions show only minor changes proving a much smaller local compression. This is in line with the results of porosity calculation (c.f. figure 5 at bottom). When comparing the development of cPSD for the different materials we find a similar set of curves for the PTFE finished materials (figure 6 B, C, E and F). In contrast, the set of cPSD graphs of the untreated material contains a significant fraction of larger pore space (note the different scaling of x-axes in figure 6 A and D).

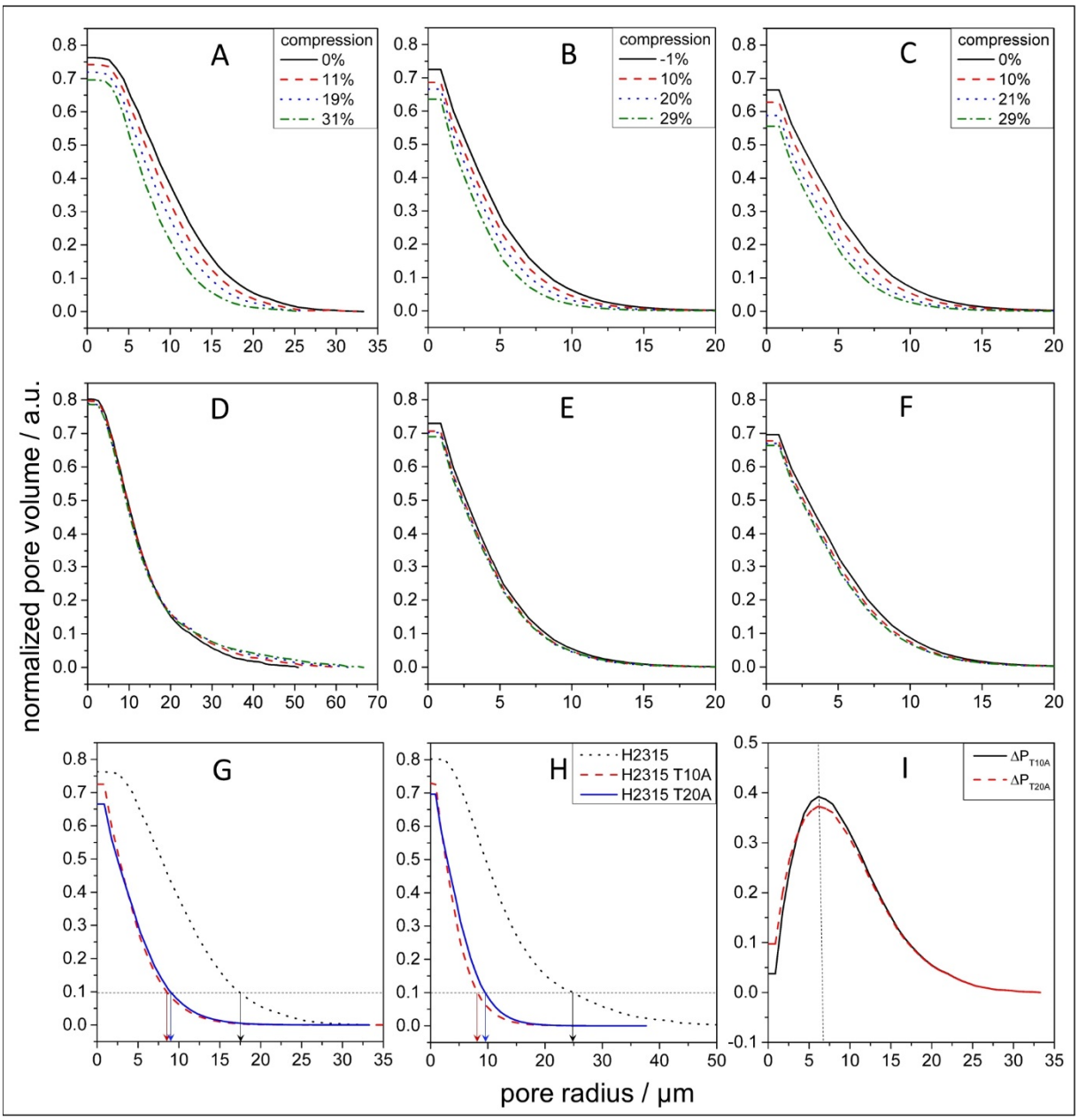

Figure 6. Continuous pore size distribution calculated for land (top row) and channel area (center row) at different degrees of compression. Plot A+D: H2315 (Note differently scaled x-axes)); Plot B+E: H2315 T10A; Plot C+F: H2315 T20A. Bottom row: Comparison of cPSD plotted for the different GDL-materials in the uncompressed state for land region (plot G) and channel region (plot H). Arrows point to the minimum radius of the largest pores that account for 10% of the total volume of respective samples. Plot I: Difference in cPSD (land) between H2315 and H2315 T10A (solid black line), H2315 and H2315 T20A (dashed red line).

In order to get a clearer comparison we plot the cPSD of the untreated and PTFE-finished material into the same chart and concentrate on the uncompressed state. To begin with the land region (see figure 6 G), only 1% of the sample volume of the PTFE finished materials (H2315 T10A and T20A) consist of pores with radii greater than 15µm. In H2315 the same continuous

pore size class accounts for about 15% of the considered sample volume. The largest pores in H2315, which account for 1% of the sample volume, have a radius of ≥ 26µm. When including pores with smaller radius that cover a volume fraction of 10% we find the corresponding radii of 8 and 8.5 µm for the finished and 17.5 µm for the untreated material. These values are marked by arrows in figure 6 G. In the channel region the differences between untreated and finished GDL-materials are even more pronounced. Considering the fractions of largest pores only, which make up for 1% of the channel volume, we find pore radii of ≥ 17 µm for the finished and ≥ 43 µm for the untreated material. When including smaller pores to reach a coverage of 10% of channel volume the corresponding pore radii are ≥ 8.5 µm for the finished and ≥ 25 µm for the untreated material (marked by arrows in figure 6 H). We can directly compare the continuous pore size distribution of considered materials by plotting its difference as shown in figure 6 I for the land region. The solid black and red dashed line show the difference between the untreated (H2315) and the PTFE-finished materials (H2315 T10A and H2315 T20A), respectively. The curves $\Delta P(r)$ reveal the difference in total volume fraction consisting of pores with the radius ≤ r. The greatest difference in the corresponding pore volumes is found at r = 6 µm. More precisely, within the land region of the untreated material the volume fraction of pore space, which can be covered by spheres (not overlapping with the solid phase) with a radius of ≤ 6 µm, is 0.39 greater than that of H2315 T10 and 0.37 greater than that of H2315 T20A. For r < 6 µm the curves of $\Delta P(r)$ decline with decreasing radius. When approaching r=0 the value of ΔP reflects the difference in porosity of the respective materials, which is 0.037 for T10A and 0.097 for T20A. In order to get a measure that describes the degree of shifts with regard to continuous pore sizes of the pore space we take the difference of $\Delta P_{max} - \Delta P(r \rightarrow 0)$. This difference tells us that 35% of total volume of H2315 that was filled with pores with a radius ≥ 6µm has been converted into pore space with pore radii < 6 µm as result of PTFE treatment in H2315 T10A. In the case of T20A only 27% of the volume is converted accordingly indicating that the sample with higher PTFE content features a slightly higher fraction of large pores. This is also indicated by the intersection of the respective cPSD curves as observable in figure 6 G. Generally, it can be stated that PTFE-finishing of H2315 leads to a shift of continuous pore size towards smaller pores, whereby especially pores with r ≥ 6 µm are converted into smaller pore spaces.

Another important structural characteristics with respect to the transport of water and gas is the tortuosity of the pathways through the pore phase. We investigated the geometric tortuosity of the pore space in through-plane direction, which is defined as the Euclidean length of the shortest paths of a geometric 3D graph representing all possible paths through the pore phase

divided by the material thickness (in *z*-direction). The geometric 3D graph of the pore phase is computed using the skeletonization algorithm implemented in the software Avizo 7. The course of the paths is determined by the skeletonization of the pore phase, i.e. the pathways follow the central axes of pores. The mean values and standard deviations of geometric tortuosity of the materials under study were calculated for land and channel regions. No significant differences between land and channel areas and no obvious correlation of geometric to the degree of compression were found. Ranging between 1.45 and 1.55 the mean tortuosity of H2315 and H2315 T10 is very similar. Ranging between 1.55 and 1.65 the mean tortuosity of the material H2315 T20A is slightly higher. An overview on this results is provided in the supplementary material (figure S3).

In the next step we calculated the in-plane tortuosity in x- and y-direction, which is an important parameter for the lateral media transport. It turned out that the mean in-plane tortuosity is basically the same for finished materials T10A and T20A independent of the considered direction (x or y) and the degree of compression (c.f. supplementary material figure S4). The mean values of in-plane tortuosity are slightly lower compared to the through plane direction suggesting good conditions for lateral media transport. In plane tortuosity for the untreated and finished materials fluctuates around 1.25, i.e. the PTFE treatment does not influence this parameter.

So far, we have described the in-plane tortuosity in terms of mean values and standard deviation only since fibers are randomly orientated on local scale. However, on a larger scale there exists a superlattice as shown in figure 7 A and already reported in [73]. It can be clearly seen that bundles of horizontally oriented fibers run almost in parallel to the x-axis in periodic distances of about 0.5 mm. This pattern results from a production step of the GDL in which fibers are hydro-entangled by water jets in z-direction in order to provide the fiber construct with mechanical stability. To analyze the influence of this regular superstructure on the local transport characteristic, we plot the mean local x-tortuosity of individual percolation paths over y-axis. The corresponding calculation domain is marked by the red rectangle in figure 7 A. The scatter plot resembles a sinus pattern as underlined by the red fitting curve (see figure 7 B). The mean local x-tortuosity fluctuates between 1.15 and 1.35 with a periodicity of 500 µm. The tortuosity minima (indicating straight transport paths) are found where fibers run in parallel bundles. The tortuosity maxima are located at the center between those bundles (marked by dot-dashed figure 7 A). Such pattern of fluctuating local tortuosity is only found in y-direction. This observation is in line with a study by Fishman et al. who considered the local porosity distribution in Freudenberg H2315 and found an oscillation in one in-plane direction. The local

peaks of this oscillation were 500 µm apart.[74] When it comes to assembling the cell one should, therefore, consider the mounting direction of the GDL sheet.

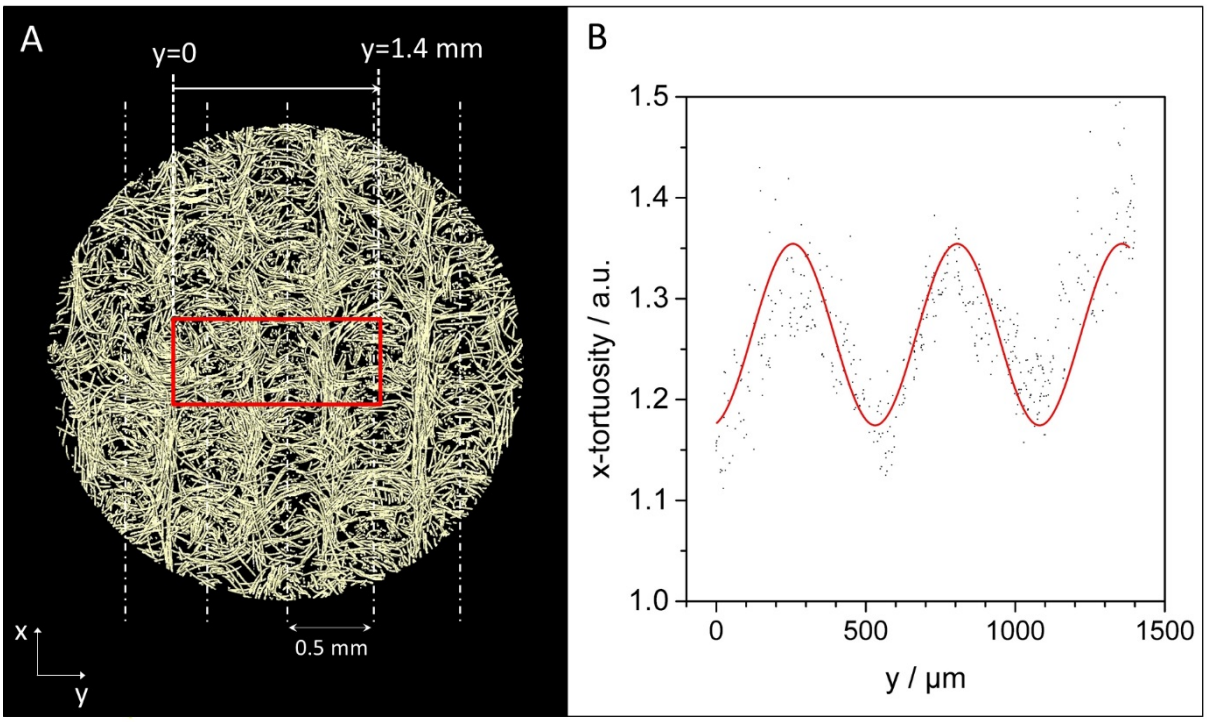

Figure 7. A: Visualization of a 50 µm thick layer extracted from the center of the GDL sample showing the superstructure of nearly parallel orientated fibers. B: Mean local x-tortuosity plotted over y direction. A single point of the scatter-plot represents the local x-tortuosity of the GDL, the starting point of the respective transport path was randomly chosen in the z-y plane. The calculation domain is marked by a red rectangle in A.

So far we have looked at the geometric tortuosity which describes how windy the transport routes through the porous material are. This parameter, however, does not yet consider cross-sectional dimensions of paths which determine capillary pressure and flow resistance. According to the Young-Laplace equation ($p_c = \frac{2\gamma \cdot cos\vartheta}{r}$) the capillary pressure depends on the water surface tension γ, the contact angle ϑ between solid and liquid phase, i.e. the wettability, and is inversely proportional to the radius of capillary [75]. Furthermore, according to the Poiseuille law the pressure drop of a liquid flowing (laminar) through a cylindrical channel is inversely proportional to the 4th power of channel radius [76]. Water is transported through the GDL material via a series of pores which are interconnected by throats [77, 78]. Therefore, it is reasonable to assume that these throats dominate the transport capacity of the path in terms of capillary pressure (that needs to be overcome for water breakthrough) and flow resistance of the flooded pathway. For this reason, we extend the calculation of geometric tortuosity by introducing a bottleneck criterion. A minimum lateral distance R_{min} between pore axis and the solid phase is required in order to be accepted as uninterrupted transport path. If a bottleneck

smaller than R_{min} is found along the pathway the path is discarded. In figure 8, the calculated mean geometric tortuosity in through-plane direction is plotted for three bottleneck limits (R_{min}= 1, 5 and 10 µm) together with the corresponding through-plane connectivity, i.e. the portion of possible paths that is found to be continuous at the chosen restriction. The top row describes the uncompressed materials, the bottom row the same materials at a compression of 30 vol.%. For the uncompressed state the considered materials show the similar trend. An increase in R_{min} leads to a smaller number of continuous pathways which have a greater mean tortuosity (connectivity sinks, mean tortuosity rises). The drop in connectivity between R_{min} = 5 µm and R_{min} = 10 µm tells us that the majority of possible pathways are restricted by bottlenecks within this dimensional range. This decrease in connectivity is most pronounced for the untreated material H2315. Only 6% of the paths fulfill the R_{min} = 10 µm criterion compared to 28% and 18% for H2315 T10A and H2315 T20A, which indicates that by far more wide transport paths are available in the PTFE-treated material. This seemingly paradox for the uncompressed state (PTFE occupies pore space) can be explained when recalling that the "uncompressed state" already includes a precompression of 0.025 MPa, as explained in section 2.3. Most of the wide transport paths in the untreated material are already constricted by this precompression whereas in H2315 T10A and T20A more wide paths remain continuous due to the enhanced mechanical strength of the fiber construct provided by PTFE-treatment. These paths play a major role as preferred transfer routes for the removal of liquid water from the catalyst layer as they feature low transport resistance [58, 79].

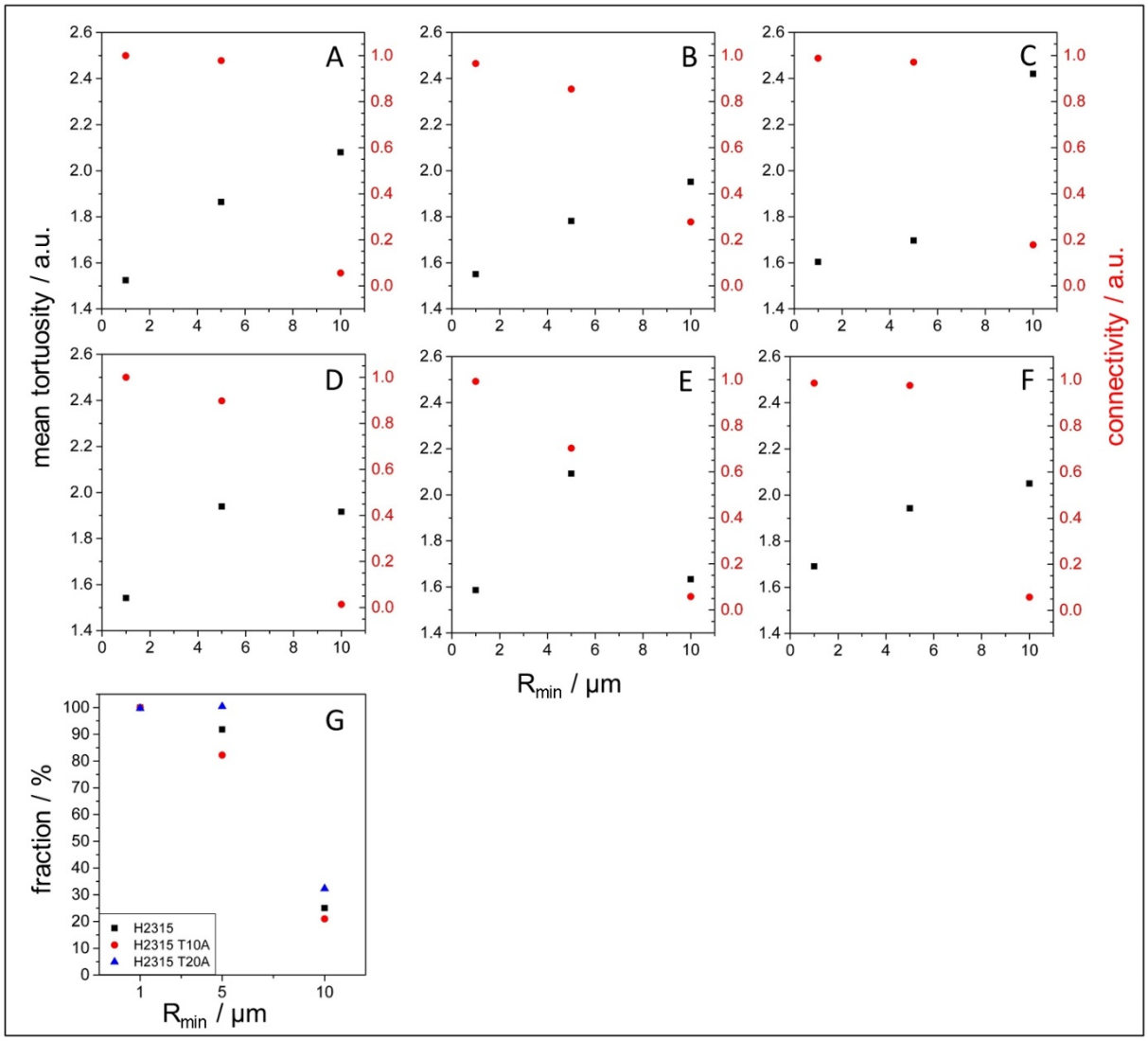

Figure 8. Mean geometric tortuosity at different radius limitations R_{min} of percolation paths (black rectangles) and the respective through-plane connectivity (red circles) plotted for the uncompressed state (top row) and a compression of 30 vol.% (center row). A+D: H2315; B+E: H2315 T10A; C+F: H2315 T20A. G: Fraction of percolation paths that remain continuous after compression by 30 vol.% considering different bottleneck sizes.

For the compressed state no obvious correlation between R_{min} and geometric mean tortuosity is found (figure 8, center row). As in the uncompressed state an increase in R_{min} leads to a smaller number of continuous pathways. However, this decrease is much more pronounced indicating that compression particularly affects the wide transport paths, thus, reduces the transport capacity for liquid water. This can be illustrated by plotting the percentage of transport paths (with reference to the uncompressed state) that still fulfill the bottleneck criterion after compression by 30 vol.% (figure 8, bottom row). For example, in case of the material H2315 T10A only 21% of wide paths (fulfilling the criterion R_{min} = 10 µm) are still left. Though compression decreases the number of wide transport paths for all considered materials, this

effect is most pronounced for the untreated material H2315: after compression only 1% of available pathways fulfill the bottleneck criterion R=10µm compared to 6% in the case of H2315 T10a and T20A (c.f. connectivity plotted in figure8, center row.). This result indicates that the PTFE treatment enhances the availability of low resistance transport paths in the compressed GDL material improving its transport capability for water.

4. Summary and Conclusions

The transport properties of fiber based GDL materials can be adjusted by adding hydrophobic agents such as polytetrafluoroethylene (PTFE). So far, the resulting improvements have been solely attributed to the modified surface properties, namely the increase of contact angle achieved by the hydrophobic treatment. In this work, we analyze the influence of PTFE treatment on the shape and microstructure of inhomogeneously compressed gas diffusion layers and discussed potential consequences for the water and media transport. Focusing on the felt type material H2315 we studied samples with increasing PTFE loads: 0, 10 and 20 wt.%. We could show that the hydrophobic agent markedly influences the 3D structure of the considered GDL materials. PTFE tends to agglomerate in between the carbon fibers. It glues fiber junctions and converts individual fibers into fiber strands which results in an enhanced mechanical strength of the fiber construct. This leads to improvements of the shape of the compressed GDL such as smoother surface and a greatly mitigated fiber intrusion into the flowfield channel. On the other hand also transport-relevant parameters of the 3D structure are affected by the treatment: Upon compression more wide transport paths remain continuous as compared to the untreated materials which strongly improves the availability of low resistance transport routes for water. The main findings of the comparative study are:

1. The hydrophobic agent is not uniformly distributed within the material. It is concentrated within the surface-near layers while the interior of the GDL contains much less PTFE. For material H2315 T10A (10 wt.% PTFE) this applies only to the top surface whereas in T20A (20 wt.% PTFE) it found at top and bottom surface.
2. Additional SEM-measurements reveal that individual fibers are not covered by a continuous film. The hydrophobic agent rather agglomerates between fibers gluing fiber junctions or connecting adjacent fibers with parallel orientation to strands.
3. PTFE coating of H2315 results in changes in microstructure and shape upon compression by a punch mimicking the flowfield geometry.

4. PTFE treatment enhances the stiffness of the fiber material leading to a different GDL shape under compression: the material extends less far (only 1/3 penetration depth) into the flowfield channel compared to the untreated GDL. However, local compression of all considered materials is markedly lower underneath the flowfield channel compared to land areas where it is in direct contact with the compression punch.
5. Fiber endings penetrating the flowfield channel form potential obstacles for moving droplets promoting the agglomeration of liquid water in the fuel cell. PTFE treatment results in a smoother GDL surface and prevents the protrusion of loose fiber endings. This was similarly observed for H2315 T10A and T20A.
6. Significant differences in pore size distribution were observed. In general, the PTFE treatment shifted the cPSD towards smaller pores. Surprisingly, this shift was slightly more pronounced for the material with lower PTFE load (T10A).
7. We found only a minor influence of compression on the geometric tortuosity in through-plane direction for all materials under study.
8. A regular superlattice that originated from a production step (water entanglement) was identified that resulted in a fluctuation of local in-plane tortuosity.
9. The transport through the majority of possible pathways is restricted by bottlenecks with a radius ranging from 5 µm to 10 µm. Upon compression the connectivity of wide paths drops, i.e. the water transport capacity sinks. However, it appears that PTFE treatment markedly mitigates this effect. In the compressed state (30vol%) the number of available wide transport paths (fulfilling the bottleneck criterion R_{min}=10µm) is 6 times greater in the PTFE-treated materials H2315 T10A and T20A than in H2315 containing no PTFE.

Exploiting the superior brilliance of a synchrotron X-ray beam and the high spatial resolution of the associated imaging instrument we were able to reproduce the microstructure of different GDLs with great accuracy. Concerning some specific morphological traits of the PTFE-treated materials, namely the PTFE distribution at individual fiber level, we reached the resolution limit of the imaging set up. Extending the resolution by additional SEM-measurements it was, however, possible to provide a very comprehensive image of the GDL-morphology under realistic compression conditions and its modification by hydrophobic treatment. The findings of this study suggest that the change in the surface characteristics, namely the increased contact angle, is not the sole reason for the modified transport behavior of PTFE-finished GDL

materials. Also the impact of hydrophobic treatment on the 3D microstructure is significant and the consequences for the liquid water transport cannot be neglected. In particular the 3D distribution of the hydrophobic agent within the material, which depends on the applied coating and drying procedure, can have a significant influence on the local microstructure and on the mechanical properties of the GDL. Optimized surface finishing procedures should, therefore, include strategies to adjust the distribution of the hydrophobic agent within the material in order to specifically change the mechanical traits of the porous material.

Acknowlegdements

We gratefully acknowledge funding of the present research by the German Federal Ministry for Education and Science (BMBF) under grant numbers 05M10KTA, 05M10CJA, 05M10VUA, and 05M10DAA. We thank our technician Holger Kropf for taking SEM-images.

Supplementary material

Table S1. Specifications of GDL types under study as provided by the manufacturer [downloadable e.g. at http://www.quintech.de/englisch/products/research/GDL-Non-woven.php]

Item Features	**H2315**	**H2315 T10 A**	**H2315 T20 A**
Hydrophobic treatment:		X	X
MPL:	No	No	No
Area weight in [g/m²]: (DIN EN ISO 29073-1)	95	105	115
TP electrical resistance at 0,6 MPa in [mΩcm²]: (internal)	7	20	45
IP electrical resistance in [Ω]: (internal)	0,8	1,0	0,9
TP air permeability* in [l/m²s]: (DIN EN ISO 9273)	400	300	300

IP air permeability in [µm²]: (internal)	5,5	3,5	3,5
Tensile strength in [N/50mm]: (DIN EN ISO 29073-3)	25	60	80

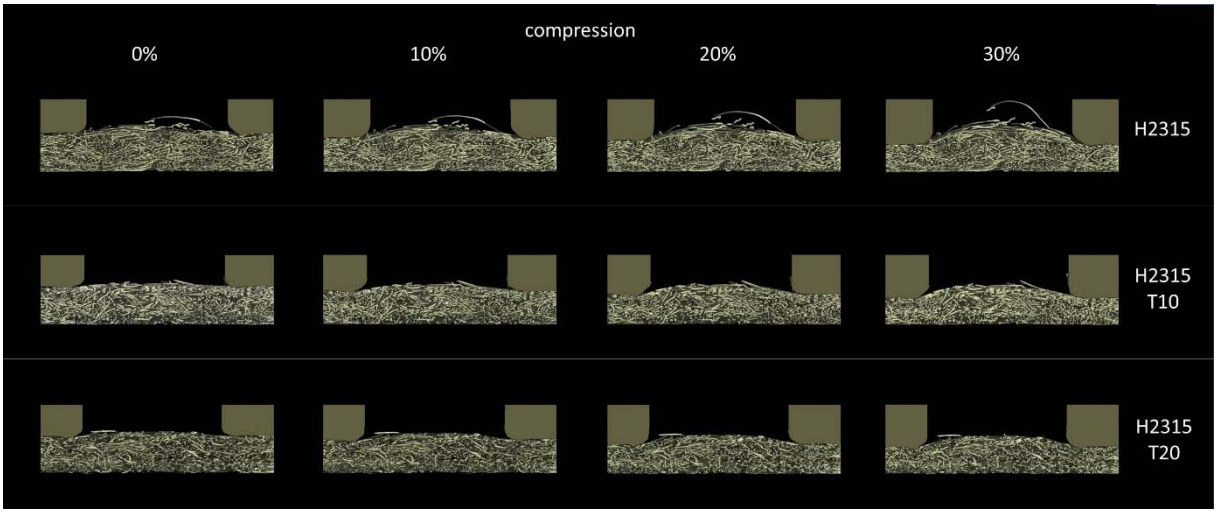

Figure S1. Image series illustrating progressive GDL extension into flowfield channel with increasing compression

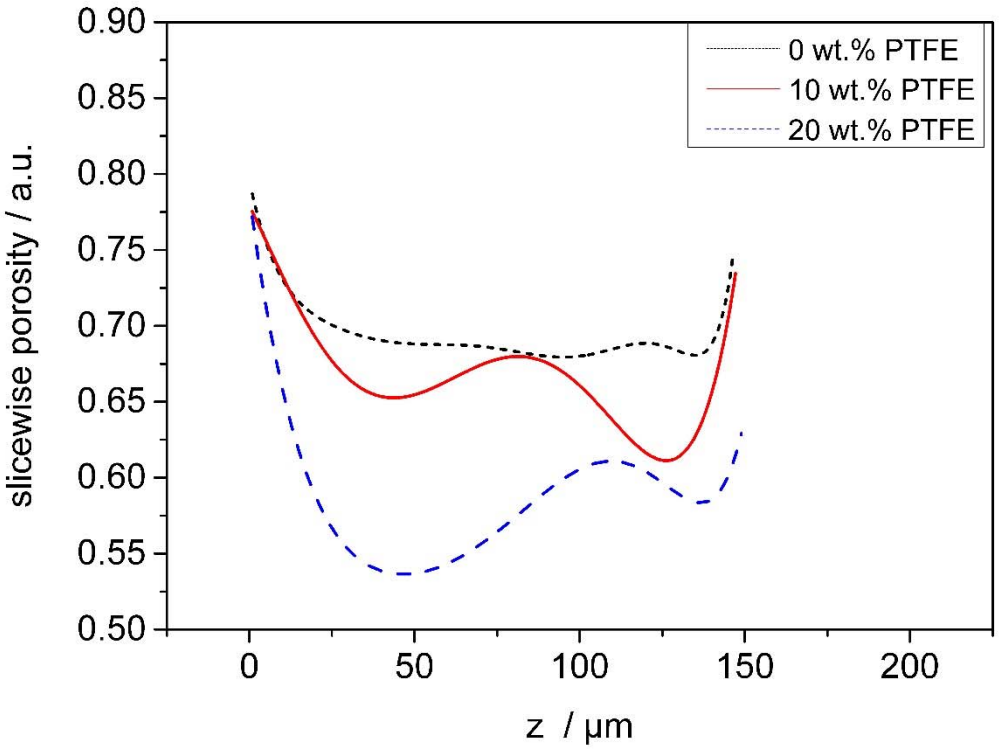

Figure S2. Local porosity different material depth (in x-y plane underneath land) at a degree of compression of 30 % (plotted from bottom up).

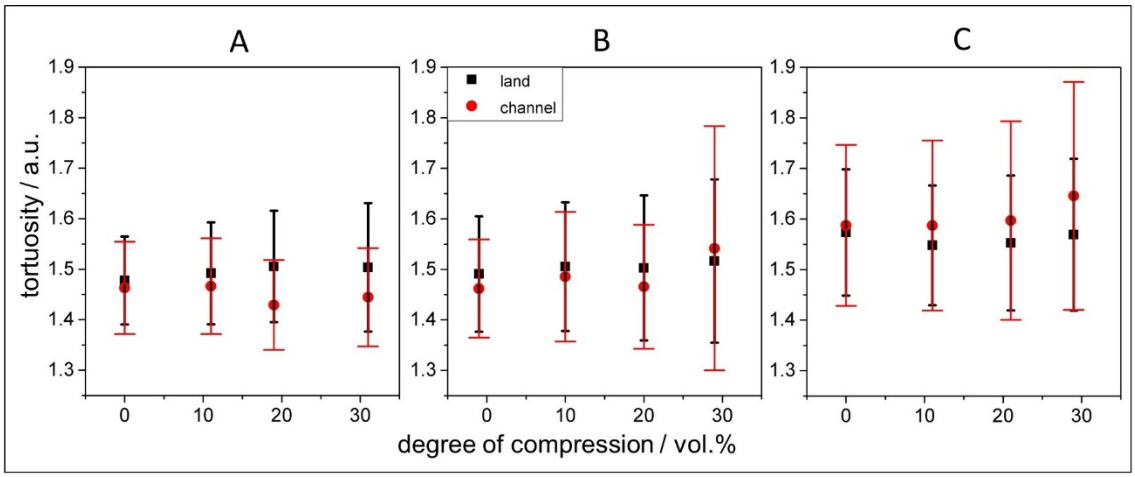

Figure S3. Mean geometric tortuosity calculated in through-plane (z-) direction at different degrees of compression. A: H2315; B: H2315 T10A; C: H2315 T20A.

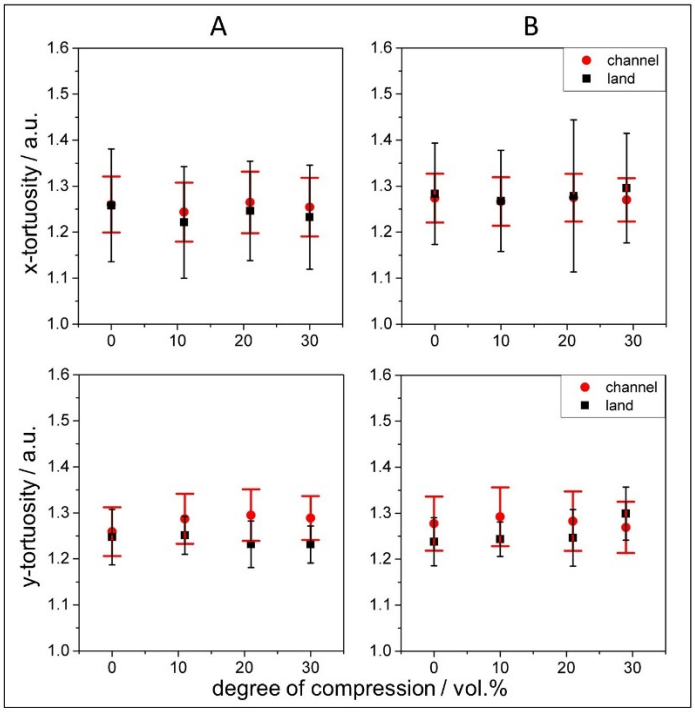

Figure S4. Mean geometric tortuosity calculated in in-plane (x- and y-) direction at different degrees of compression. A: H2315 T10A, B: H2315 T20A

Further information on procedures used in the geometrical analysis

The local porosity of sample was calculated as function of material depth. We used the binarized data of the reconstructed sample volume and evaluated the proportion of pores and fibers for every tomographic slice within the considered land regions. The resulting set of points was fitted using higher degree polynomials. The uncertainty of this measurements is mainly correlated to the accuracy of binarization procedure and is estimated to be lower than 5%.

To determine penetration depth of GDL into the channel we considered 0.1 mm wide channel section around the centerline of the flow field channel. For each considered degree compression we identified the horizontal layer in which the proportion of fibers was 5% within the considered section. The penetration depth was calculated as the vertical distance of this layer from the channel edge. The uncertainty of measurement is related to the spatial resolution of the measurement and is estimated to be lower than 5 µm.

The continuous pore size distribution (cPSD) does not consider pores as discrete objects but treats the entire pore structure as continuum. It describes the fraction of the pore volume P(r) that can be covered by spheres with a radius r, such that these spheres do not overlap with the solid (fiber) phase. To calculate the cPSD we used the algorithm suggested by Munch et. al. This algorithm simulates an intrusion process of a spherical droplet which starts from the pore locations which represent local maxima of the pore size. By incrementally reducing the radius of the intruding liquid, pores with lower dimensions can be filled successively. A continuous PSD is then obtained by integration of the infiltrated volume over the corresponding range of radii. For a more detailed mathematical description of the cPSD we refer to [71]. The uncertainty of this measurements is mainly correlated to the accuracy of binarization procedure and is estimated to be lower than 5%.

The geometric tortuosity of the pore space in a given direction is defined as the Euclidean length of the shortest paths of a geometric 3D graph that represents all possible paths through the pore phase divided by the material thickness (in the considered direction).The geometric 3D graph of the pore phase is computed using the skeletonization algorithm implemented in the software Avizo 7. In brief, this algorithm first calculates a distance map of the segmented image, then performs a thinning of the labelfield such that finally a string of connected voxels remains. The voxel skeleton is then converted to a spatial graph object. The distance to the nearest boundary is stored at every point of the spatial graph as thickness attribute. This also allows for applying bottleneck criteria to investigate transport-relevant radius restrictions along a path. This criteria states that a minimum lateral distance R_{min} between pore axis and the solid phase is required in order to be accepted as uninterrupted transport path. If a bottleneck smaller than R_{min} is found along the pathway the path is discarded. For more a more detailed description we refer to the manual of AVIZO 7. The uncertainty of this measurements is mainly correlated to the accuracy of binarization procedure and is estimated to be lower than 5%.

References

[1] C.-Y. Wang, Two-phase flow and transport, in: W. Vielstich, A. Lamm, H.A. Gasteiger (Eds.) Handbook of Fuel Cells – Fundamentals, Technology and Applications, John Wiley & Sons, Chichester, 2003, pp. 337–347.

[2] P.K. Sinha, P.P. Mukherjee, C.Y. Wang, Journal of Materials Chemistry, 17 (2007) 3089-3103.

[3] W. Vielstich, A. Lamm, H.A. Gasteiger, in: Handbook of Fuel Cells – Fundamentals, Technology and Applications

John Wiley & Sons, Chichester, 2003.
[4] M.F. Mathias, J. Roth, J. Fleming, W. Lehnert, Diffusion media materials and characterisation, in: Handbook of Fuel Cells, John Wiley & Sons, Ltd, 2010.
[5] J. Millichamp, T.J. Mason, T.P. Neville, N. Rajalakshmi, R. Jervis, P.R. Shearing, D.J.L. Brett, Journal of Power Sources, 284 (2015) 305-320.
[6] A. Bazylak, D. Sinton, Z.S. Liu, N. Djilali, Journal of Power Sources, 163 (2007) 784-792.
[7] E.H. Lehmann, P. Boillat, G. Scherrer, G. Frei, Nuclear Instruments and Methods in Physics Research Section A: Accelerators, Spectrometers, Detectors and Associated Equipment, 605 (2009) 123–126.
[8] R.J. Bellows, M.Y. Lin, M. Arif, A.K. Thompson, D. Jacobson, Journal of The Electrochemical Society, 146 (1999) 1099-1103.
[9] R. Satija, D.L. Jacobson, M. Arif, S.A. Werner, Journal of Power Sources, 129 (2004) 238-245.
[10] I. Manke, C. Hartnig, M. Grunerbel, J. Kaczerowski, W. Lehnert, N. Kardjilov, A. Hilger, J. Banhart, W. Treimer, M. Strobl, Applied Physics Letters, 90 (2007) 184101.
[11] C. Hartnig, I. Manke, N. Kardjilov, A. Hilger, M. Grünerbel, J. Kaczerowski, J. Banhart, W. Lehnert, Journal of Power Sources, 176 (2008) 452-459.
[12] J.P. Owejan, T.A. Trabold, D.L. Jacobson, D.R. Baker, D.S. Hussey, M. Arif, International Journal of Heat and Mass Transfer, 49 (2006) 4721-4731.
[13] A. Santamaria, H.-Y. Tang, J.W. Park, G.-G. Park, Y.-J. Sohn, International Journal of Hydrogen Energy, 37 (2012) 10836-10843.
[14] P. Boillat, D. Kramer, B.C. Seyfang, G. Frei, E. Lehmann, G.G. Scherer, A. Wokaun, Y. Ichikawa, Y. Tasaki, K. Shinohara, Electrochemistry Communications, 10 (2008) 546-550.
[15] D. Kramer, J. Zhang, R. Shimoi, E. Lehmann, A. Wokaun, K. Shinohara, G.G. Scherer, Electrochimica Acta, 50 (2005) 2603-2614.
[16] P. Boillat, G. Frei, E.H. Lehmann, G.G. Scherer, A. Wokaun, Electrochemical and Solid-State Letters, 13 (2010) B25-B27.
[17] C. Totzke, I. Manke, A. Hilger, G. Choinka, N. Kardjilov, T. Arlt, H. Markotter, A. Schroder, K. Wippermann, D. Stolten, C. Hartnig, P. Kruger, R. Kuhn, J. Banhart, Journal of Power Sources, 196 (2011) 4631-4637.
[18] H. Markotter, I. Manke, R. Kuhn, T. Arlt, N. Kardjilov, M.P. Hentschel, A. Kupsch, A. Lange, C. Hartnig, J. Scholta, J. Banhart, Journal of Power Sources, 219 (2012) 120-125.
[19] M. Klages, S. Enz, H. Markotter, I. Manke, N. Kardjilov, J. Scholta, Journal of Power Sources, 239 (2013) 596-603.
[20] T. Arlt, W. Lueke, N. Kardjilov, J. Banhart, W. Lehnert, I. Manke, Journal of Power Sources, 299 (2015) 125-129.
[21] T. Arlt, A. Schroeder, K. Heyne, H. Riesemeier, K. Wippermann, W. Lehnert, I. Manke, Journal of Power Sources, 297 (2015) 83-89.
[22] M.A. Hoeh, T. Arlt, I. Manke, J. Banhart, D.L. Fritz, W. Maier, W. Lehnert, Electrochemistry Communications, 55 (2015) 55-59.
[23] A. Lange, A. Kupsch, M.P. Hentschel, I. Manke, N. Kardjilov, T. Arlt, R. Grothausmann, Journal of Power Sources, (2010).
[24] A. Turhan, K. Heller, J.S. Brenizer, M.M. Mench, Journal of Power Sources, 160 (2006) 1195-1203.
[25] J.M. LaManna, S. Chakraborty, J.J. Gagliardo, M.M. Mench, International Journal of Hydrogen Energy, 39 (2014) 3387-3396.
[26] K.T. Cho, M.M. Mench, Physical Chemistry Chemical Physics, 14 (2012) 4296-4302.
[27] I. Manke, C. Hartnig, M. Grunerbel, W. Lehnert, N. Kardjilov, A. Haibel, A. Hilger, J. Banhart, H. Riesemeier, Applied Physics Letters, 90 (2007) 174105.
[28] I. Manke, H. Markötter, C. Tötzke, N. Kardjilov, R. Grothausmann, M. Dawson, C. Hartnig, S. Haas, D. Thomas, A. Hoell, C. Genzel, J. Banhart, Advanced Engineering Materials, 13 (2011) 712-729.
[29] S.R. Stock, International Materials Reviews, 53 (2008) 129-181.

[30] J.P. James, H.W. Choi, J.G. Pharoah, International Journal of Hydrogen Energy, 37 (2012) 18216-18230.
[31] J. Becker, R. Flückiger, M. Reum, F.N. Büchi, F. Marone, M. Stampanoni, Journal of The Electrochemical Society, 156 (2009) B1175-B1181.
[32] R. Kuhn, J. Scholta, P. Krueger, C. Hartnig, W. Lehnert, T. Arlt, I. Manke, Journal of Power Sources, 196 (2011) 5231-5239.
[33] I.V. Zenyuk, D.Y. Parkinson, G. Hwang, A.Z. Weber, Electrochemistry Communications, 53 (2015) 24-28.
[34] S.H. Eberhardt, M. Toulec, F. Marone, M. Stampanoni, F.N. Buechi, T.J. Schmidt, Journal of the Electrochemical Society, 162 (2015) F310-F316.
[35] T. Sasabe, S. Tsushima, S. Hirai, International Journal of Hydrogen Energy, 35 (2010) 11119-11128.
[36] T. Sasabe, P. Deevanhxay, S. Tsushima, S. Hirai, Journal of Power Sources, 196 (2011) 8197-8206.
[37] T. Sasabe, P. Deevanhxay, S. Tsushima, S. Hirai, Electrochemistry Communications, 13 (2011) 638-641.
[38] A. Bazylak, International Journal of Hydrogen Energy, 34 (2009) 3845-3857.
[39] J. Hinebaugh, J. Lee, A. Bazylak, Journal of The Electrochemical Society, 159 (2012) F826-F830.
[40] J. Lee, J. Hinebaugh, A. Bazylak, Journal of Power Sources, 227 (2013) 123-130.
[41] W. Maier, T. Arlt, K. Wippermann, C. Wannek, I. Manke, W. Lehnert, D. Stolten, Journal of The Electrochemical Society, 159 (2012) F398-F404.
[42] H. Markotter, J. Haussmann, R. Alink, C. Totzke, T. Arlt, M. Klages, H. Riesemeier, J. Scholta, D. Gerteisen, J. Banhart, I. Manke, Electrochemistry Communications, 34 (2013) 22-24.
[43] A.B. Geiger, A. Tsukada, E. Lehmann, P. Vontobel, A. Wokaun, G.G. Scherer, Fuel Cells, 2 (2002) 92-98.
[44] N. Pekula, K. Heller, P.A. Chuang, A. Turhan, M.M. Mench, J.S. Brenizer, K. Ünlü, Nuclear Instruments and Methods in Physics Research Section A: Accelerators, Spectrometers, Detectors and Associated Equipment, 542 (2005) 134-141.
[45] P.K. Sinha, P. Halleck, C.-Y. Wang, Electrochemical and Solid-State Letters, 9 (2006) A344-A348.
[46] M.A. Hickner, N.P. Siegel, K.S. Chen, D.S. Hussey, D.L. Jacobson, M. Arif, Journal of The Electrochemical Society, 155 (2008) B427-B434.
[47] C. Hartnig, I. Manke, R. Kuhn, S. Kleinau, J. Goebbels, J. Banhart, Journal of Power Sources, 188 (2009) 468-474.
[48] I. Manke, C. Hartnig, N. Kardjilov, H. Riesemeier, J. Goebbels, R. Kuhn, P. Krüger, J. Banhart, Fuel Cells, 10 (2010) 26-34.
[49] K. Seidenberger, F. Wilhelm, J. Haußmann, H. Markötter, I. Manke, J. Scholta, Journal of Power Sources, 239 (2013) 628-641.
[50] J. Lee, R. Yip, P. Antonacci, N. Ge, T. Kotaka, Y. Tabuchi, A. Bazylak, Journal of the Electrochemical Society, 162 (2015) F669-F676.
[51] G. Gaiselmann, R. Thiedmann, I. Manke, W. Lehnert, V. Schmidt, Computational Materials Science, 59 (2012) 75-86.
[52] H. Markotter, R. Alink, J. Haussmann, K. Dittmann, T. Arlt, F. Wieder, C. Totzke, M. Klages, C. Reiter, H. Riesemeier, J. Scholta, D. Gerteisen, J. Banhart, I. Manke, International Journal of Hydrogen Energy, 37 (2012) 7757-7761.
[53] N. Kardjilov, I. Manke, A. Hilger, M. Strobl, J. Banhart, Materials Today, 14 (2011) 248-256.
[54] L. Gondek, N.B. Selvaraj, J. Czub, H. Figiel, D. Chapelle, N. Kardjilov, A. Hilger, I. Manke, International Journal of Hydrogen Energy, 36 (2011) 9751-9757.
[55] K. Herbrig, C. Pohlmann, L. Gondek, H. Figiel, N. Kardjilov, A. Hilger, I. Manke, J. Banhart, B. Kieback, L. Roentzsch, Journal of Power Sources, 293 (2015) 109-118.
[56] C. Pohlmann, K. Herbrig, L. Gondek, N. Kardjilov, A. Hilger, H. Figiel, J. Banhart, B. Kieback, I. Manke, L. Roentzsch, Journal of Power Sources, 277 (2015) 360-369.
[57] P. Krüger, H. Markötter, J. Haussmann, M. Klages, T. Arlt, J. Banhart, C. Hartnig, I. Manke, J. Scholta, Journal of PowerSources, 196 (2011) 5250-5255.

[58] H. Markötter, I. Manke, P. Krüger, T. Arlt, J. Haussmann, M. Klages, H. Riesemeier, C. Hartnig, J. Scholta, J. Banhart, Electrochemistry Communications, 13 (2011) 1001-1004.
[59] J. Haussmann, H. Markotter, R. Alink, A. Bauder, K. Dittmann, I. Manke, J. Scholta, Journal of Power Sources, 239 (2013) 611-622.
[60] J. Eller, T. Rosen, F. Marone, M. Stampanoni, A. Wokaun, F.N. Buchi, Journal of The Electrochemical Society, 158 (2011) B963-B970.
[61] R. Flückiger, F. Marone, M. Stampanoni, A. Wokaun, F.N. Büchi, Electrochimica Acta, 56 (2011) 2254-2262.
[62] T. Rosen, J. Eller, J. Kang, N.I. Prasianakis, J. Mantzaras, F.N. Buchi, Journal of The Electrochemical Society, 159 (2012) F536-F544.
[63] J. Eller, J. Roth, F. Marone, M. Stampanoni, A. Wokaun, F.N. Buechi, Journal of Power Sources, 245 (2014) 796-800.
[64] N. Khajeh-Hosseini-Dalasm, T. Sasabe, T. Tokumasu, U. Pasaogullari, Journal of Power Sources, 266 (2014) 213-221.
[65] C. Tötzke, G. Gaiselmann, M. Osenberg, J. Bohner, T. Arlt, H. Markötter, A. Hilger, F. Wieder, A. Kupsch, B.R. Müller, M.P. Hentschel, J. Banhart, V. Schmidt, W. Lehnert, I. Manke, Journal of Power Sources, 253 (2014) 123-131.
[66] W. Görner, M.P. Hentschel, B.R. Müller, H. Riesemeier, M. Krumrey, G. Ulm, W. Diete, U. Klein, R. Frahm, Nuclear Instruments and Methods in Physics Research Section A: Accelerators, Spectrometers, Detectors and Associated Equipment, 467-468 (2001) 703-706.
[67] G. Gaiselmann, C. Tötzke, I. Manke, W. Lehnert, V. Schmidt, Journal of Power Sources, 257 (2014) 52-64.
[68] S.H. Williams, A. Hilger, N. Kardjilov, I. Manke, M. Strobl, P.A. Douissard, T. Martin, H. Riesemeier, J. Banhart, Journal of Instrumentation, 7 (2012) P02014.
[69] A. Lange, M.P. Hentschel, A. Kupsch, B.R. Müller, International Journal of Materials Research, 103 (2012) 174-178.
[70] C. Tötzke, I. Manke, G. Gaiselmann, J. Bohner, B.R. Müller, A. Kupsch, M.P. Hentschel, V. Schmidt, J. Banhart, W. Lehnert, Review of Scientific Instruments, 86 (2015) 043702.
[71] B. Münch, L. Holzer, Journal of the American Ceramic Society, 91 (2008) 4059-4067.
[72] L. Holzer, B. Münch, M. Rizzi, R. Wepf, P. Marschall, T. Graule, Applied Clay Science, 47 (2010) 330-342.
[73] G. Gaiselmann, D. Froning, C. Tötzke, C. Quick, I. Manke, W. Lehnert, V. Schmidt, International Journal of Hydrogen Energy, 38 (2013) 8448-8460.
[74] Z. Fishman, J. Hinebaugh, A. Bazylak, Journal of The Electrochemical Society, 157 (2010) B1643-B1650.
[75] A.W. Adamson, A.P. Gast, (1967).
[76] S.P. Sutera, R. Skalak, Annual Review of Fluid Mechanics, 25 (1993) 1-20.
[77] P.K. Sinha, C.-Y. Wang, Electrochimica Acta, 52 (2007) 7936-7945.
[78] A. Bazylak, V. Berejnov, B. Markicevic, D. Sinton, N. Djilali, Electrochimica Acta, 53 (2008) 7630-7637.
[79] P. Zhou, C.W. Wu, Journal of Power Sources, 195 (2010) 1408-1415.